Topology Optimization of Pressure Adaptive Honeycomb for a Morphing Flap

Roelof Vos[a], Jan Scheepstra[a], and Ron Barrett[b]
[a]Faculty of Aerospace engineering, Delft University of Technology, Delft, The Netherlands;
[b]Dept. of Aerospace Engineering, The University of Kansas, Lawrence, KS 66045

ABSTRACT

The paper begins with a brief historical overview of pressure adaptive materials and structures. By examining avian anatomy, it is seen that pressure-adaptive structures have been used successfully in the Natural world to hold structural positions for extended periods of time and yet allow for dynamic shape changes from one flight state to the next. More modern pneumatic actuators, including FAA certified autopilot servoactuators are frequently used by aircraft around the world. Pneumatic artificial muscles (PAM) show good promise as aircraft actuators, but follow the traditional model of load concentration and distribution commonly found in aircraft. A new system is proposed which leaves distributed loads distributed and manipulates structures through a distributed actuator. By using Pressure Adaptive Honeycomb (PAH), it is shown that large structural deformations in excess of 50% strains can be achieved while maintaining full structural integrity and enabling secondary flight control mechanisms like flaps. The successful implementation of pressure-adaptive honeycomb in the trailing edge of a wing section sparked the motivation for subsequent research into the optimal topology of the pressure adaptive honeycomb within the trailing edge of a morphing flap. As an input for the optimization two known shapes are required: a desired shape in cruise configuration and a desired shape in landing configuration. In addition, the boundary conditions and load cases (including aerodynamic loads and internal pressure loads) should be specified for each condition. Finally, a set of six design variables is specified relating to the honeycomb and upper skin topology of the morphing flap. A finite-element model of the pressure-adaptive honeycomb structure is developed specifically tailored to generate fast but reliable results for a given combination of external loading, input variables, and boundary conditions. Based on two bench tests it is shown that this model correlates well to experimental results. The optimization process finds the skin and honeycomb topology that minimizes the error between the acquired shape and the desired shape in each configuration.

Keywords: Pressure Adaptive, Honeycomb, Cellular Structure, Pneumatic, Morphing

1. INTRODUCTION

Aircraft structures are challenged by many requirements, foremost among them are typically weight, strength and stiffness. Flight control systems and structures have many additional requirements including control authority, power consumption and bandwidth. In the natural world, flight control systems are made from comparatively stiff structural elements (bones) which are moved relative to each other by comparatively compliant chemical-to-mechanical energy transducers (muscles). If one sifts through the fossil record of flying animals and examines the anatomy of many avians of today, a slightly different type of secondary flight control actuator can be seen. These structural elements use air pressure for maintenance of shape, structural integrity, compliance manipulation and control. Indeed recent discoveries in flying dinosaur anatomy point to large structural air sacs in pterosaurs which were used to manipulate large body parts and even smaller organelles in wing skins.[1-4] Birds (and crocodilians) of today have more highly evolved versions of these ancient organs. These modern animals respire by ingesting air, then moving the air through a series of air sacs and lengthy structures, some of which can carry loads. These structures are used to hold body parts in a particular shape for extended periods of time, then allow the same body parts to hold a different form when called upon to do so.

Secondary aircraft flight control systems of today have similar requirements; indeed, flaps are typically slightly extended for take-off, fully retracted during cruise and mostly extended for landing. In the same way that avians need to hold particular wing shapes depending on flight state, airplane secondary flight control surfaces must be held in position for long periods of time while absorbing airloads of varying magnitudes from different directions. Although most flight control actuators use hydraulic or electromechanical mechanisms to move structures, the aerospace industry has more than a half-century of experience with pneumatic flight control systems.[5] These aircraft pneumatic flight control systems employed air-powered gyros which were connected to air pressure manipulation systems, which in turn were connected

Active and Passive Smart Structures and Integrated Systems 2011, edited by Mehrdad N. Ghasemi-Nejhad,
Proc. of SPIE Vol. 7977, 79771J · © 2011 SPIE · CCC code: 0277-786X/11/$18 · doi: 10.1117/12.880359

to pneumatic servos. The servos drove push-rods back and forth to move flight control surfaces. Several advantages of the Britain pneumatic autopilot systems include low weight and power consumption, simplicity, high reliability and the ability to function in parallel with a human pilot without either triggering an autopilot auto-disconnect or overriding mechanical commands from the pilot.

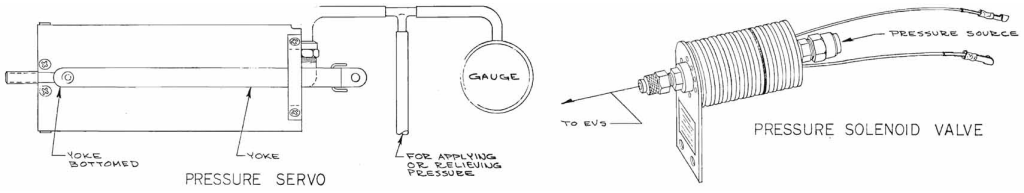

Figure 1 FAA Certified, Fielded, Brittain Industries, Inc. Aircraft Autopilot Pressure Servo and Solenoid Valve[5]

Because pneumatic actuators have many favorable properties, a number of investigators have been using them as robotics actuators. Some of the newest forms of pneumatic actuators are taking the form of "pneumatic artificial muscles" (PMA).[6] Although PMA's cannot yet match the force-stroke (total work) capability of conventional piston-cylinder actuators, their solid state nature is a good selling point for certain applications. Recent technologists have applied PMAs to a variety of helicopter flight control surfaces with good results.[7-9]

Although PMA's and conventional pneumatic cylinders have certain undeniable advantages over conventional approaches, as discrete actuators they still require finite hard points on primary structure. As has been the case for more than a hundred years of human flight control, distributed airloads are absorbed by a given flight control surface and concentrated at hinge points, flap track pulleys, push rods, wires, crank arms and other discrete points. The loads at these points are then redistributed along primary structure of the aircraft and transferred to the rest of the airframe. This overall scheme of taking distributed loads, concentrating them to run through an actuator, then redistributing them is not very efficient from a weight perspective and typically leads to flight control surface weights being double or triple the amount of a similarly sized fixed aircraft structure.

Although this general arrangement of flight control systems is nearly universal, a new philosophy in control actuation has evolved over the past five years. The fundamental idea of this flight control arrangement is to absorb distributed loads, leave them distributed as they pass through a distributed actuator, then transfer them in a distributed state to primary structure. In not concentrating loads, there are significant weight savings to be had over conventional approaches. To make this happen, a new form of adaptive material is necessary to use. This type of adaptive material uses pneumatic pressure much in the same way that it is used in the natural world in that it keeps structural loads locally low, while distributing loads over a large area within the surface. By varying the pressure inside of cylindrical structural pockets of aircraft-grade honeycomb, it has been shown that very high stress, strain and active work densities can be achieved as shown in Figure 2:

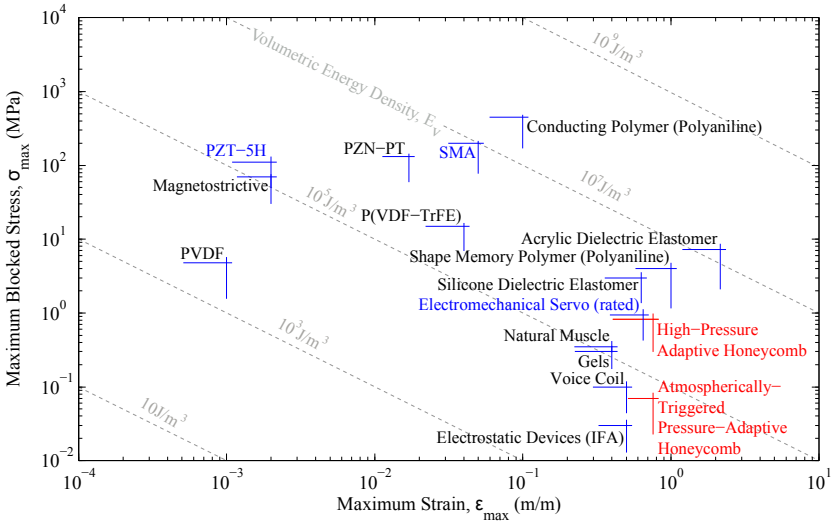

Figure 2 adaptive materials blocked stress, maximum strain and work density[10]

This Pressure Adaptive Honeycomb (PAH) has been employed in single cells, lines of cells, multicellular expanding units, skinned multicellular bending units and wing sections.[10-13] Following successful build-up, several experiments on wing sections in wind tunnels showed good, predictable deflections with both airspeed and angle of attack. These early studies were centered on simply proving the concept. No effort at optimization was made at all. Basic correlation of theory and experiment showed promise with good results. Still, structural weights, local strain levels and activity levels could be improved. Accordingly, it is the purpose of this paper to demonstrate a method for analytically optimizing pressure adaptive honeycomb actuators in a generic flap system.

2. DESIGN TOOL FOR A PRESSURE ADAPTIVE MORPHING FLAP

2.1 Morphing Flap Structural Optimization Objective

The objective of the present research is to generate a feasible design for a pressure-adaptive morphing flap. The resulting design should be relatively easy to manufacture and operate. Therefore, the number of design variables for the topology of the flap has been limited. For example, it has been assumed that all the honeycomb cells are pressurized at the same cell differential pressure (CDP), that all the cells have the same initial manufacturing geometry (θ_i), and that the manufacturing curvature, (κ) of the top skin should be constant. Having a constant CDP over all the cells allows for a single pressure tube to connect to a high-pressure source within the aircraft, reducing the complexity of the system. The constant curvature of the top skin allows for an easy manufacturing process of the top skin (rolling). Finally, the constant honeycomb angle also allows for automated manufacturing of the honeycomb cells, which keeps production costs low.

With these manufacturing and implementation constraints, the values of the aforementioned variables, in addition to the skin thickness distribution, $t(x)$, and the honeycomb cell wall length, l, should be determined such that two target shapes are approximated as closely as possible. For the two target shapes it is assumed that an aerodynamic analysis has preceded the structural design of the flap. Based on the aerodynamic analysis an optimum shape in landing and cruise conditions is assumed along with the target pressure distribution in each condition. The optimum shape in landing condition is termed the 'high-lift' shape, while the optimum shape in cruise condition is referred to as the 'cruise' shape. The two target shapes share a common center section, which represents the rigid torque box structure. The morphing parts of the flap section are the leading and trailing edge. In the present design, only the trailing edge topology is considered.

2.2 Description of the Design Tool

In Figure 3 a step-by-step process of the design tool is visualized. The output of the design tool is the manufacturing shape of the skin (both in terms of curvature and thickness distribution), the manufacturing topology of the honeycomb (initial honeycomb angle and cell wall length), and the CDPs that should be applied in high-lift and cruise conditions. Based on this output the adaptive flap can be manufactured and the required maximum CDP has been established.

In the first step of the procedure, the flap target shapes are identified. An aerodynamic analysis should also result in a design pressure distribution over the top and bottom surface of the flap. These pressure distributions are an important input for the morphing flap, because the inherent flexibility has been shown to result in aeroelastic deformation under aerodynamic loading.[13] In order to get to the target shape in the design condition, it is therefore important that the pressure distribution is known beforehand.

In the second step the designer determines which part of the morphing trailing edge is going to be filled with honeycomb cells. From experience it has been concluded that it is not necessary for successful morphing to occupy the entire trailing edge with honeycomb cells. Therefore, a solid tip is included in the design. The solid tip is an input that is defined as a fraction of the total flap chord. The space between the solid tip and the aft spar is subsequently automatically meshed with hexagonal cells of a specified length (l) and honeycomb angle (θ_i).

In step 3 the forces are calculated over the top skin. From step 1, the pressures on the top and bottom skin are known. However, in the present design case, the pressure difference between the top and bottom surface is calculated and the resulting pressure is mapped onto the top skin. This is done to simplify the analysis, as is explained in Section 3. The bottom skin is not considered in the present design tool. In step 3, the pressure over the solid tip is consolidated into a single force at the end of the honeycomb section denoted with F_{tip}. The result is two distinct pressure distributions, tip forces, and target shapes for the pressure adaptive honeycomb section.

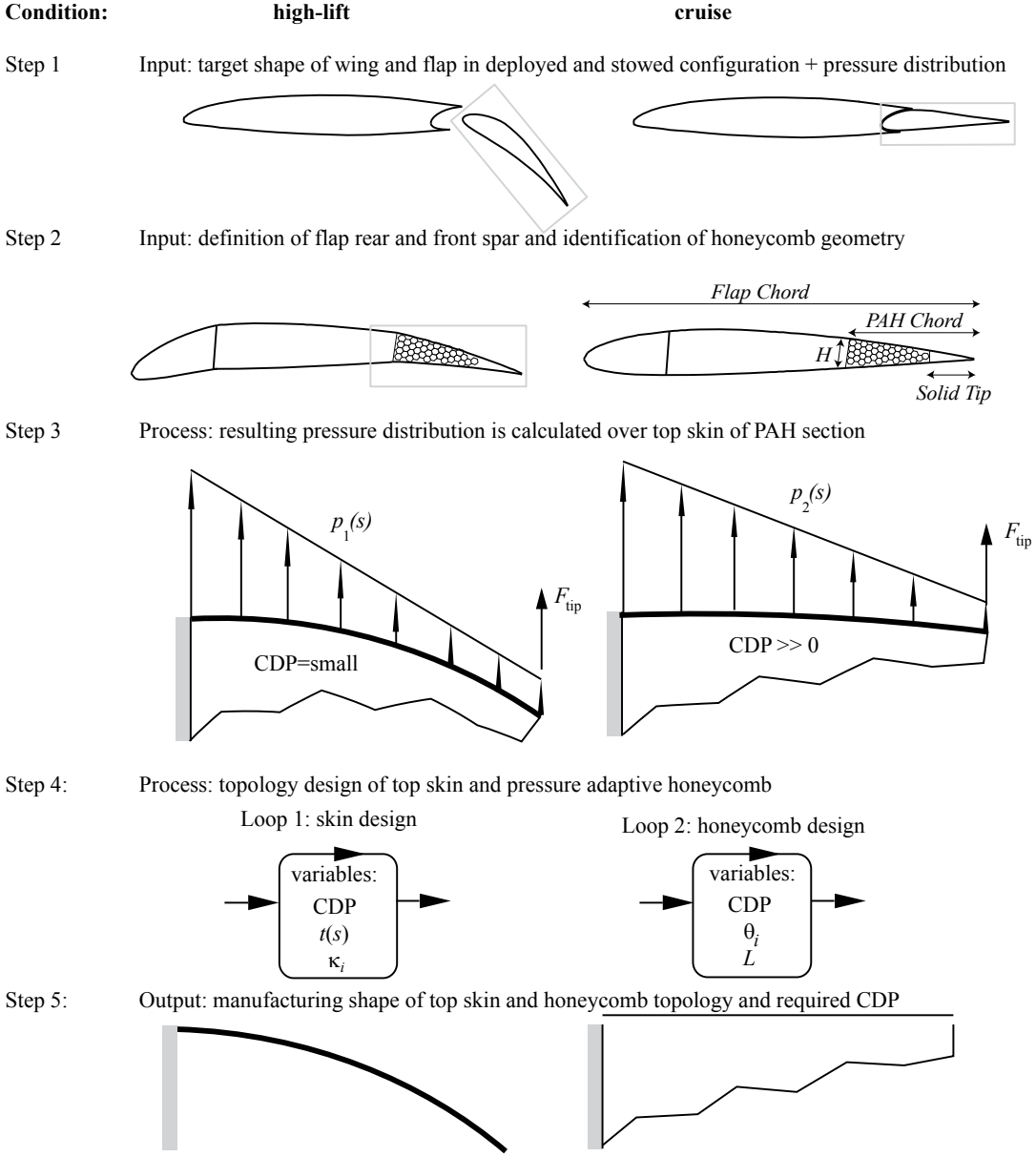

Figure 3 Step-by-step process in the topology design of a pressure-adaptive morphing flap

In step 4 the optimization process is started in order to identify for what design variables the two target shapes are most closely matched. Additional input parameters are defined such as CDP (in both conditions), $t(x)$, and κ. A finite element (FE) analysis is carried out that determines the resulting shape under the external aerodynamic load and the internal CDP at each condition. The resulting shape of the top skin is compared to the target shape and an error is calculated. This process is carried out for the two different conditions. In the high-lift conditions it is presumed that the CDP is very low and that the shape is dominated by the balance between aerodynamic loads and skin bending. Therefore only the skin parameters are altered in this design loop. When the error between the calculated shape and the target shape is below a predefined value, the loop is stopped and the skin variables are fixed. The second design loop is started with a different load condition and target shape. In this condition the CDP should be responsible for most of the deformation and is therefore included as a design variable. When a particular combination of the design variables results in a shape close enough to the target shape the loop is terminated.

In step 5 the output parameters are presented. For the skin this implies a manufacturing geometry in terms of curvature and thickness distribution. For the PAH a honeycomb angle and a wall length is defined. In addition, the CDP in high-lift and cruise conditions is determined which is important for operating requirements of the morphing structure.

2.3 Present Limitations and Further Improvements

The presented design tool is a starting point for a structural design engineer to design the internal structure of a morphing flap. However, in its present form there are still some limitations:

- The bottom skin of the adaptive flap is not included. A practical implementation of the present morphing flap would benefit from a flexible skin on the pressure surface of the flap. This skin would be able to transfer the pressure load to the solid tip and the root of the PAH section, leading to a different external load case than presently considered.
- There is no aeroelastic coupling between the structural model and the aerodynamic model. Only in the design case do the shapes and pressure distributions match between the two models. Moreover, the morphing process from one configuration to the other cannot be evaluated at the moment.
- Important constraints on maximum skin deformation (in terms of yield limits) are not included in the optimization process.

The above limitations are subject of further improvements of the design tool. However, it is shown in Section 4 that the present design tool can be used to generate feasible design results.

3. FINITE ELEMENT ANALYSIS

The finite element analysis of the pressure-adaptive honeycomb forms the core of the structural design tool. Based on a simplified model of the honeycomb and the skin, rapid evaluations of the various designs can be produced.

3.1 Model Setup and Assumptions

The present model assumes that the flexible honeycomb material can be approximated by rigid walls connected by frictionless hinges. For a thin-walled honeycomb cell it has been observed that the largest curvature change occurs near the folds, leaving the largest part of the cell wall uncurved. As long as the deformation stays in the linear realm the kinematics of flexible honeycomb are quite well approximated by rigid-wall honeycombs.

For pressure-adaptive honeycomb the enclosed volume of the cell correlates to the stiffness of the pressurized honeycomb structure. In the practical application of the pressure adaptive honeycomb it is anticipated that each hexagonal cell inhabits a pouch that forms a circular tube within the hexagonal cells when the CDP is increased. This pouch is not explicitly modeled. This implies that the pressure-induced stiffness of the structure is overestimated in the present analysis. It can be shown that the pressure-induced stiffness should be reduced with 9% to account for the unpressurized volume within the honeycomb grid.[10]

The FE model is build up from Total Lagrangian (TL) bar elements. By using TL bars, the displacements of each individual bar can be calculated in a local reference frame and later converted to the global reference frame and added to the corresponding nodes. Due to the infinite bending stiffness of the bars, elongation is the only deformation possible. All bars are connected to nodes of the global honeycomb grid. These nodes are represented as frictionless hinges. Figure 4 shows the used definition of a TL bar with respect to local and global coordinates.

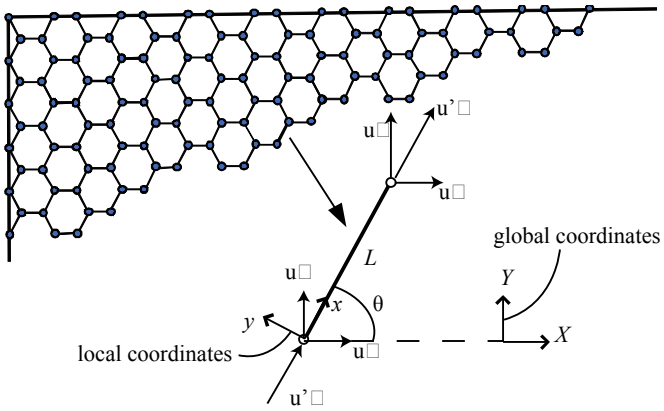

Figure 4 Finite element definition of pressure adaptive honeycomb: bars connected by hinges

The total energy potential of the system (Π) is the difference between the strain energy potential, U, and the external loads potential, V:

$$\Pi = U - V \tag{1}$$

While U only considers the strain in the bar elements, V is related to the aerodynamic loads, the loads that are introduced by the curved skin, and the loads generated by the CDP. The conservative internal ($\bar{p}$) and external ($\bar{f}$) forces in the system can be found by taking the first derivative of the potential functions:

$$\frac{\partial \Pi}{\partial \bar{u}} = \frac{\partial U}{\partial \bar{u}} - \frac{\partial V}{\partial \bar{u}} = \bar{p} - \bar{f} = \bar{r} \tag{2}$$

The displacement of each node, $\mathrm{d}\bar{u}$, is a function of the residual force vector, $\bar{r}$, and the global stiffness matrix, $\bar{\bar{K}}$:

$$\mathrm{d}\bar{u} = \frac{\bar{\bar{K}}}{\bar{r}} \tag{3}$$

From each bar a total of three local stiffness matrices are derived. These matrices are known as the *material stiffness matrix* ($\bar{\bar{k}}_m$), the *geometric stiffness matrix* ($\bar{\bar{k}}_g$) and the *load stiffness matrix* ($\bar{\bar{k}}_l$). Given that a FE bar has four degrees-of-freedom, these three matrices each are of size 4×4. The local stiffness matrices are then assembled into the global stiffness matrices $\bar{\bar{K}}_m$, $\bar{\bar{K}}_g$, and $\bar{\bar{K}}_l$ and subsequently combined into a single global stiffness matrix $\bar{\bar{K}}$. Matrix $\bar{\bar{K}}$ contains all inherent stiffness properties of the structure and can be derived from the potential energy functions by taking the second derivative with respect to the nodal displacement:

$$\frac{\partial^2 \Pi}{\partial \bar{u}^2} = \frac{\partial^2 U}{\partial \bar{u}^2} - \frac{\partial^2 V}{\partial \bar{u}^2} = \frac{\partial \bar{p}}{\partial \bar{u}} - \frac{\partial \bar{f}}{\partial \bar{u}} \tag{4}$$

where $\partial \bar{p}/\partial \bar{u} = \bar{\bar{K}}_m + \bar{\bar{K}}_g$ and $-\partial \bar{f}/\partial \bar{u} = \bar{\bar{K}}_l$. The stiffness matrix $\bar{\bar{K}}_l$ is the sum of the stiffness matrices stemming from the three external loads (CDP, aerodynamic loading, and skin loading):

$$\bar{\bar{K}}_l = \bar{\bar{K}}_{\mathrm{CDP}} + \bar{\bar{K}}_{\mathrm{aero}} + \bar{\bar{K}}_{\mathrm{skin}} \tag{5}$$

To calculate these three global stiffness matrices, the distributed pressures and moments are expressed as lumped forces at each of the nodes. For each bar that experiences a cell differential pressure, the pressure force is multiplied with the length and equally distributed over the end nodes. For the introduction of the skin-induced forces the resistance to bending of the skin is approximated by a set of rigid bars that are connected with torsion springs (Figure 5). Any change in curvature of the skin then results in a corrective moment produced by the torsion springs. This moment is translated to an equivalent force (F_{eq}). The torsion stiffness of the springs, k_{rot}, is correlated to the material thickness by equating the deflection of the flexible skin section to the bar deflection. The thickness of the material can therefore alter the nodal forces for a given change in curvature, $\mathrm{d}\varphi$.

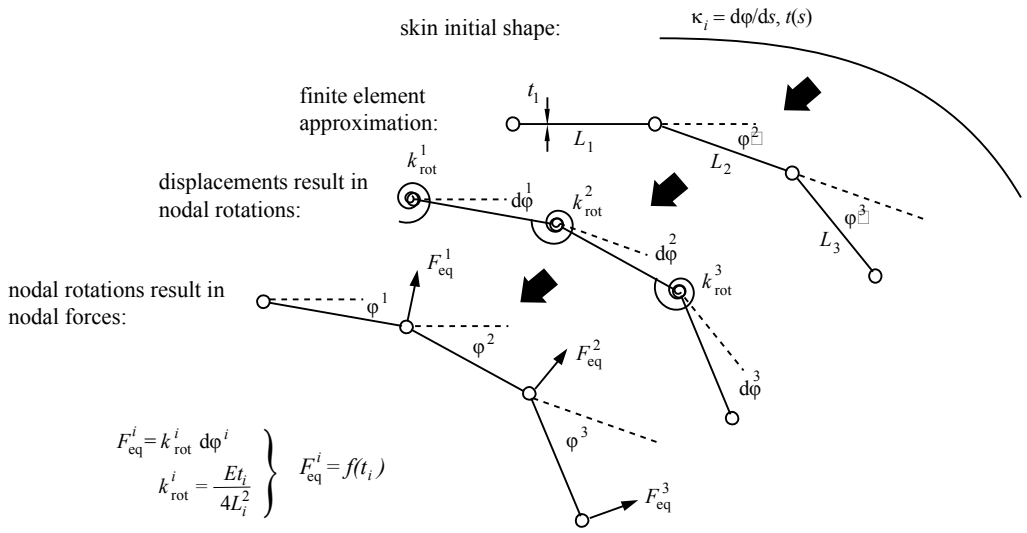

Figure 5 Nodal forces are introduced by skin bending and a function of the element thickness, t_i.

Finally, the aerodynamically-induced pressure distribution is projected on the top skin. The pressure distribution is discretized with only values at the nodes. Subsequently, this discretized pressure distribution is employed to calculate the resulting forces (P_i) perpendicular to each of the elements as shown in Figure 6. This concludes the determination of the external forces that are present on the bar elements in the skin and in the honeycomb.

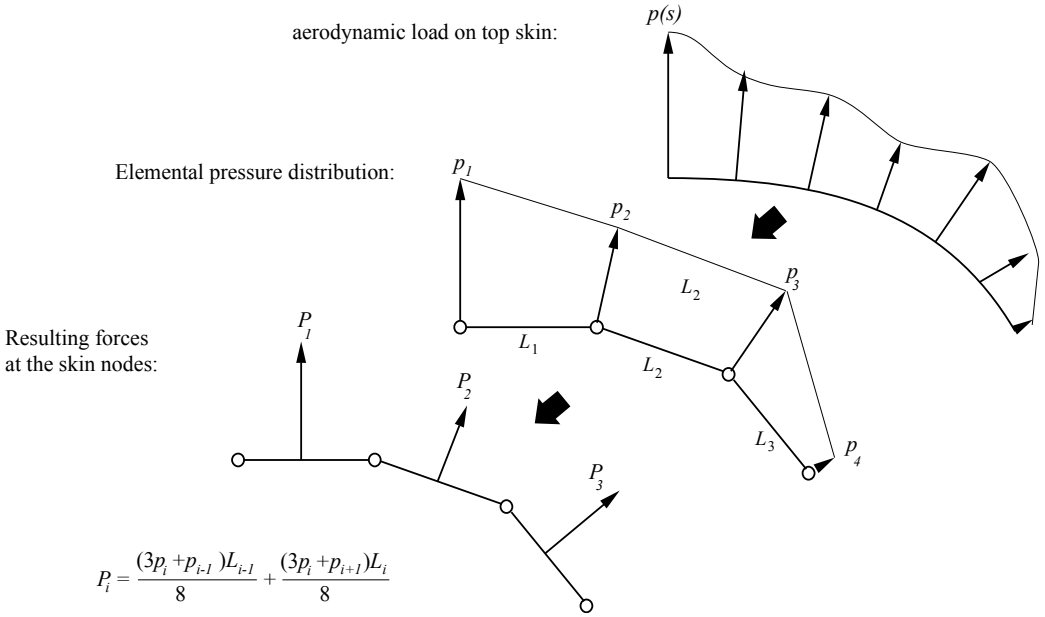

Figure 6 Element forces introduced by the aerodynamic pressure distribution on the top skin.

When the force vectors are calculated, the global stiffness matrices can be determined can be determined. These matrices are explicitly derived by Scheepstra *et al.*[14] and are presented here for clarity. The global material matrix is affected by the stiffness of the material, E, its cross-sectional area (equal to t for unit length) and the bar orientation, θ. The following stiffness matrix results, where $c = \cos\theta$ and $s = \sin\theta$:

$$\bar{\bar{K}}_m = \frac{Et}{L}\begin{bmatrix} c^2 & cs & -c^2 & -cs \\ cs & s^2 & -cs & -s^2 \\ -c^2 & -cs & c^2 & cs \\ -cs & -s^2 & cs & s^2 \end{bmatrix} \tag{6}$$

The geometric stiffness matrix accounts for the element deformation which occurs when considering finite displacements. It is based on the tension (N) in the bars and bar length and holds for nonlinear (large) displacements:

$$\bar{\bar{K}}_g = \frac{N}{L}\begin{bmatrix} 1 & 0 & -1 & 0 \\ 0 & 1 & 0 & -1 \\ -1 & 0 & 1 & 0 \\ 0 & -1 & 0 & 1 \end{bmatrix} \tag{7}$$

The global stiffness matrix due to a cell differential pressure becomes:

$$\bar{\bar{K}}_{\mathrm{CDP}} = -\frac{\partial \bar{f}_{\mathrm{CDP}}}{\partial \bar{u}} = \frac{CDP}{2}\begin{bmatrix} 0 & -1 & 0 & 1 \\ 1 & 0 & -1 & 0 \\ 0 & -1 & 0 & 1 \\ 1 & 0 & -1 & 0 \end{bmatrix} \tag{8}$$

The global stiffness matrix due aerodynamic loading is a function of the forces at the two end nodes (P_1 and P_2, respectively):

$$\bar{\bar{K}}_{\mathrm{aero}} = -\frac{\partial \bar{f}_{\mathrm{aero}}}{\partial \bar{u}} = \frac{1}{L}\begin{bmatrix} 0 & -P_1 & 0 & P_1 \\ P_1 & 0 & -P_1 & 0 \\ 0 & -P_2 & 0 & P_2 \\ P_2 & 0 & -P_2 & 0 \end{bmatrix} \tag{9}$$

Finally, the global stiffness matrix due to the bending in the skin can be related to the equivalent force vector (F_{eq}), stemming from the rotation of the skin bar elements and the torsion stiffness:

$$\bar{\bar{K}}_{\mathrm{skin}} = -\frac{\partial \bar{f}_{\mathrm{skin}}}{\partial \bar{u}} = \frac{F_{\mathrm{eq}}}{L}\begin{bmatrix} 0 & 0 & 0 & 0 \\ 0 & 0 & 0 & 0 \\ 0 & -1 & 0 & -1 \\ 1 & 0 & 1 & 0 \end{bmatrix} \tag{10}$$

Summing the individual stiffness matrices results in the global stiffness matrix that can be substituted in Equation 3 to obtain the displacement of each of the nodes for a given residual force vector, $\bar{r}$. If the coordinates at a particular iteration are denoted with subscript j, then the new coordinates are found according to:

$$u_{j+1} = u_j + \mathrm{d}u \tag{11}$$

The updated geometry results in a new residual force vector and corresponding stiffness matrix is derived and the process is repeated. This analysis loop is terminated when the following condition is reached:

$$\left|\bar{r}_{j+1} - \bar{r}_j\right| < 1 \times 10^{-10} \tag{12}$$

3.2 Comparison to Experiments

To verify the model presented in the previous section a simple tension-compression test was constructed using an electromechanical tension/compression machine (Instron model nr. 3345). A single honeycomb cell was constructed out of a 2-ply Kevlar pre-impregnated laminate. The hinges were introduced by local carbonization of the matrix structure which degraded the bending stiffness dramatically. The length of each hexagon face amounted to $L = 20$mm. Two sets of tests were carried out. In the first test the force was aligned with the specimen's x-axis (longitudinal), while in the second test the force lined up with y-axis (lateral). In both tests the specimen was loaded through its center axis such that no shear loads were introduced.

The pressure in the pouch was kept constant during the experiment by using a variable pressure unit. The experiment was carried out in a quasi static way, meaning the top chuck displaced at a rate of 5mm/minute. Pressure, tensile force, and displacement were all sampled at 1Hz. A 5000N pressure transducer was used that could measure forces as small as 1mN. Displacements were recorded with an accuracy of 1μm. A strain-based pressure transducer was employed in combination with LabVIEW 8.5 to record the CDP. The pressure transducer was calibrated using a digital manometer that was accurate up to 0.1kPa. The single cell honeycomb element measured 29cm in depth. During the test, the displacement was controlled according to a triangular wave with time. In Figure 7 the experimental setup and input signal is presented.

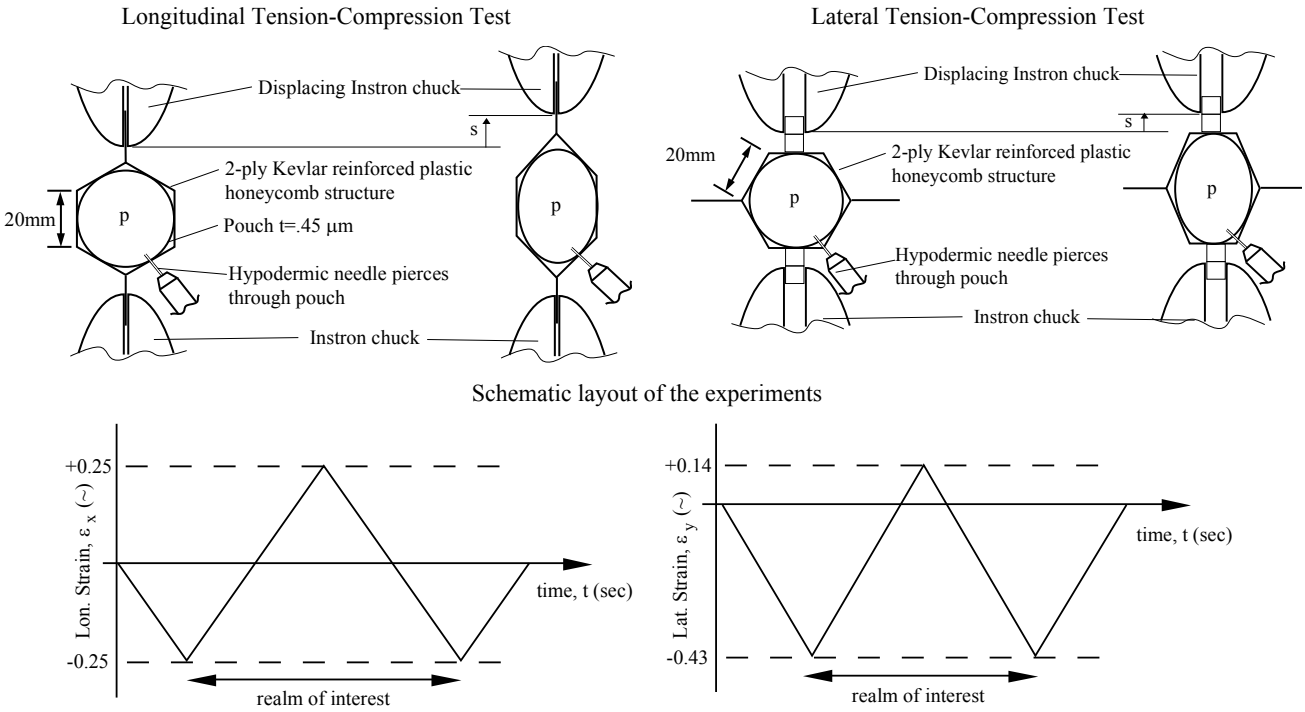

Figure 7 Experimental setup for compression-extension test of single-cell honeycomb test article

The results of the tension-compression experiments are displayed in Figure 8 along with the prediction by the FE model. In longitudinal direction, it can be seen that the model does not exactly match the experimental results. However, it does give an excellent first estimate of the force-displacement relation of pressurized honeycomb over a large range of strains (see Figure 7). It is therefore expected that for small strains, the model is able to generate quite useful results and is a good basis for the design tool that is presented in this paper.

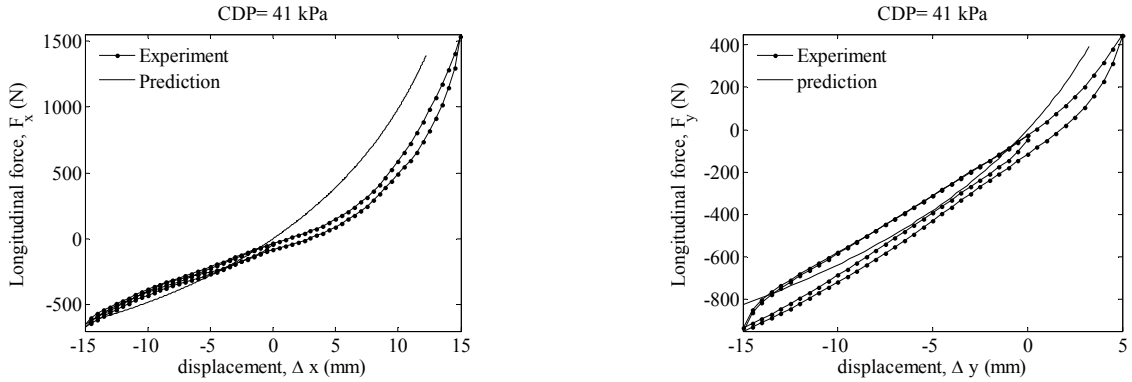

Figure 8 Comparison between prediction of FE model and the experimental results for single-cell compression-extension tests

4. DEMONSTRATION OF DESIGN TOOL

In the present section three prospective topology designs for a morphing flap are presented. The goal is to show how the design tool can be employed to investigate the effect of different honeycomb and skin topologies on the cruise and high-lift shapes of the honeycomb. In the present design tool, the two optimization loops of step 4 in Figure 3 are not yet fully employed. In total six design variables are identified: κ_i, $t(s)$, θ_i, L, $\text{CDP}_{\text{high-lift}}$, and $\text{CDP}_{\text{cruise}}$. In the prospective application of the tool some of these variables will appear as constraints, while others will be varied to fulfill an objective function (e.g. minimizing weight). However, presently only $t(s)$ is optimized in the process, while the other variables are manually altered to approach the target shape as closely as possible.

As a starting geometry a NACA 2412 profile is assumed as the cruise shape of the adaptive flap. This flap measures c_f =1000mm in length and the aft 20% ($x > 0.8c_f$) can be deformed due to CDP and aerodynamic loading. In cruise conditions, a $\text{CDP}_{\text{cruise}}$ of 200kPa is applied. In addition, it is assumed that the manufacturing curvature of the skin is $\kappa_i = 0.011$rad/m. In Table 1 the geometric and aerodynamic inputs for the two target shapes are displayed. Note that a gross simplification of the pressure distribution is used for simplification.

Table 1 Aerodynamic and geometric input for demonstration example

	high-lift condition	cruise condition
target curvature	$\kappa = 0.01$ [rad/m]	$\kappa = 0.001$[rad/m]
aerodynamic load distribution	$p_1(s) = 15.0(1 - \frac{x}{c_f})$ [kN] for $x > 0.8c_f$	$p_1(s) = 22.7(1 - \frac{x}{c_f})$ [kN] for $x > 0.8c_f$

In Table 2 the specific geometric inputs for the three different test cases are displayed. In addition a small CDP is added in the high-lift configuration in order to let the FE analysis converge. This CDP value is displayed in the last column of Table 2.

Table 2 Values of design variables for the four different test cases

Test #	start	end	L [mm]	H [mm]	θ_i [deg]	$\text{CDP}_{\text{high-lift}}$ [kPa]
1	$0.80c_f$	$0.92c_f$	22	120	55	6
2	$0.80c_f$	$0.88c_f$	10	80	58	8
3	$0.80c_f$	$0.88c_f$	8	100	56	12

With the values of the design parameters set, the target shapes identified, and the aerodynamic loading specified, the tool calculates the shape of the pressure adaptive honeycomb in each condition. For each of the test cases, the results are displayed in Figure 9 through Figure 11. In each of these figures, the target shape in each condition is also displayed and one can see how well this target shape is approached by the pressure adaptive honeycomb. The boundary conditions of the honeycomb can also be identified in these figures. The honeycomb is clamped on three sides. On the left side the honeycomb is attached to the flap structure, while on the right-hand side it attaches to the solid tip. This solid tip is represented by the truss structure attaching to the honeycomb. Finally, the honeycomb attaches to the flexible upper skin.

In the first test case (Figure 9) the honeycomb wall length is chosen comparatively large, which results in quite a large discrepancy between target shape and obtained shape in high-lift conditions. The curvature near the tip of the honeycomb cannot be attained due to the truss structure reducing the top skin curvature. This effect reduces considerably when decreasing the cell size (Figure 10 and Figure 11). The effect of the solid tip remains limited to the first cell that attaches to it. For all three cases, the desired shape in cruise is approached quite accurately. This is not surprising due to the fact that the pressurized honeycomb approaches a flat plate ($\kappa = 0$) when CDP is increased to infinity.

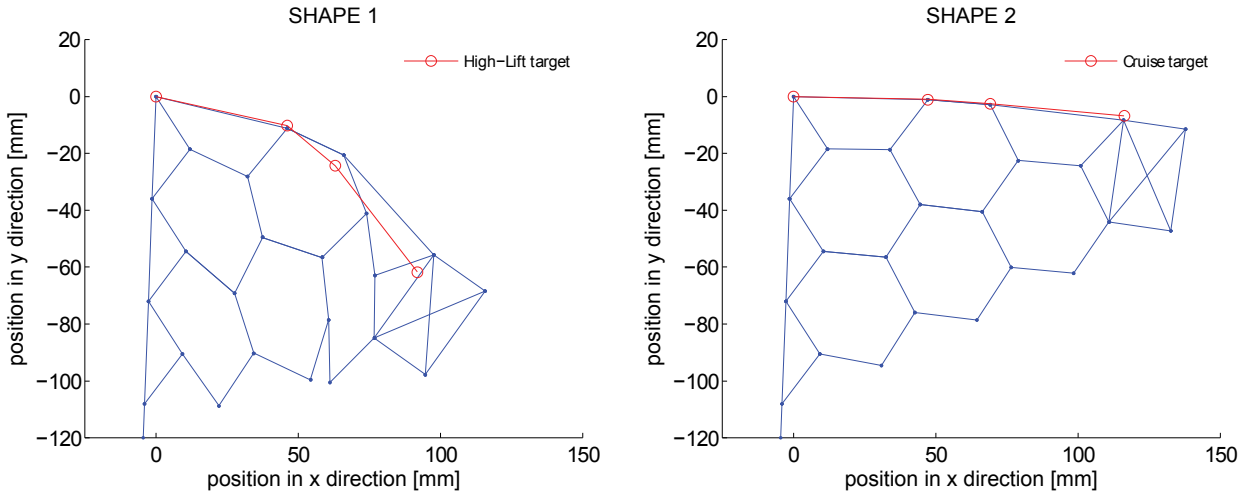

Figure 9 Results for test #1

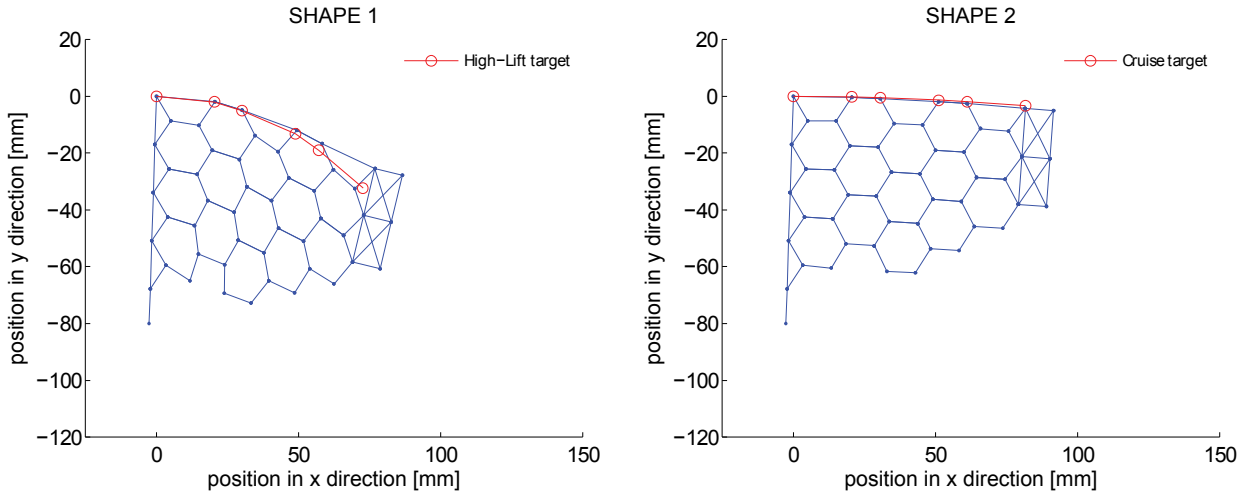

Figure 10 Results for test #2

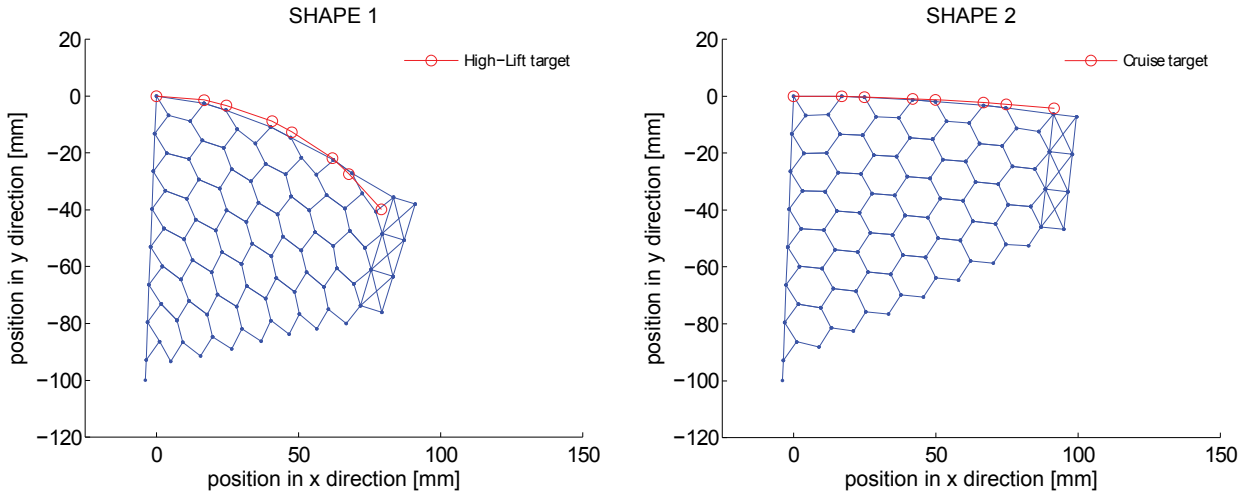

Figure 11 Results for test #3

The test results above show that for the target curvatures, a pressure-adaptive honeycomb structure can be designed that approaches these curvatures. In its present state, the simulation can be used as a 'what-if' tool to quickly investigate the result of some key parameter changes. Based on the various input parameters and the corresponding output, the designer can choose which combination of parameters yields an acceptable result, within a set of manufacturing and operating constraints. As stated in Section 4, in the near future, more variables will be determined within the tool as part of a multi-variable optimization process.

5. CONCLUSIONS

Due to the complex interaction of aerodynamic, pressure, and structural loads within pressure-adaptive honeycomb, a design tool has been developed that can be used to size the internal honeycomb structure, as well as the upper skin of the trailing edge of a pressure-adaptive morphing flap. The core of this design tool relies on a simple representation of the honeycomb structure by means of rigid members connected by frictionless hinges. Two compression-extension tests of a single-cell rigid-wall honeycomb structure demonstrated good correlation to the FE model, giving sufficient confidence that this representation could be used for the prediction of the shape of a larger, partially-constrained pressure-adaptive structure. A topology optimization strategy was developed that relied on six design variables that governed the topology of the honeycomb structure and the upper skin. This optimization strategy was partially implemented and was successfully demonstrated to show the effects of design changes on the structural performance of the structure. The tool presently works well in predicting the shape of the pressure-adaptive trailing edge in cruise and high-lift condition. It automatically calculates the associated skin thickness distribution that matches the acquired shape to the aerodynamically desired shapes in these two conditions. Future efforts are tailored towards automating the design loops even further to be able to quickly calculate the best topology for the trailing edge of a morphing flap.

ACKNOWLEDGEMENTS

The authors would like to acknowledge the valuable advice of Dr. Markus Pagitz with respect to the implementation a Finite-element model in the design tool. Furthermore, the authors would like to acknowledge the support of the Transport Research Institute of The University of Kansas for providing the authors the ability to investigate pressure adaptive honeycombs and its applications.

REFERENCES

[1] Claessens, L.P.A.M., O'Conner, P.M., and Unwin, D.M., "Respiratory Evolution Facilitated the Origin of Pterosaur Flight and Aerial Gigantism," PLoS ONE, 4(2), e4497 (2009).

[2] Farmer, C.G. and Sanders, K., "Unidirectional Airflow in the Lungs of Alligators," Science, 327(5963), 338-340 (2010).

[3] Hicks, J.W. and White, F.N., "Pulmonary gas exchange during intermittent ventilation in the American alligator," Respiratory Physiology, 88(23) (1992).

[4] O'Conner, P.M. and Claessens, L.P.A.M., "Basic avian pulmonary design and flow-through ventilation in non-avian theropod dinosaurs," Nature, 436, 253-256 (2005).
[5] Anon., "Constant Co-Pilot Operation and Service Instructions Model BSA-4 Pressure System, Manual No. 3966," Brittain Industries, a Division of Narco Scientific Industries, Torrence, CA, 1968.
[6] Chou, C. and Hannaford, B., "Static and dynamic characteristics of McKibben pneumatic artificial muscles," IEEE International Conference on Robotics and Automation, San Diego, CA, IEEE, Vol. 1, 281-286 (1994).
[7] Bubert, E., Woods, B., Sirohi, J., Kothera, C.S., and Wereley, N., "Whirl Testing of Pneumatic Artificial Muscle Systems for Helicopter Rotor Applications," ASME International Design Engineering Technical Conference, Las Vegas, NV, ASME (2007).
[8] Woods, B., Kothera, C.S., and Wereley, N., "Whirl Testing of a Pneumatic Artificial Muscle Driven Helicopter Trailing Edge Flap," American Helicopter Society Annual Forum (2008).
[9] Yerkes, N. and Wereley, N., "Pneumatic Artificial Muscle Activation for Trailing Edge Flaps," 46th AIAA Aerospace Sciences Meeting, Reno, NV, AIAA-2008-1418 (2008).
[10] Vos, R. [Mechanics and Applications of Pressure Adaptive Honeycomb], Dissertation, The University of Kansas, Lawrence, KS (2009).
[11] Vos, R. and Barrett, R., "Pressure Adaptive Honeycomb: a New Adaptive Structure for Aerospace Applications," Proceedings of SPIE Smart Structures and Materials Conference, San Diego, CA, SPIE, Vol. 7647 (2010).
[12] Vos, R. and Barrett, R., "Pressure Adaptive Honeycomb: Mechanics, Modeling and Experimental Investigation," 18th AIAA/ASME/AHS Adaptive Structures Conference, Orlando, FL, AIAA-2010-2664 (2010).
[13] Vos, R. and Barrett, R., "Applications and Mechanics of Pressure Adaptive Honeycomb," 3rd ASME Conference on Smart Materials, Adaptive Structures and Intelligent Systems, Philadelphia, PA, ASME (2010).
[14] Scheepstra, J., Vos, R., and Barrett, R., "Topology Design of Pressure Adaptive Honeycomb for a Morphing Fowler Flap," 19th AIAA/ASME/AHS Adaptive Structures Conference, AIAA (2011).